Nanoscale

PAPER

View Article Online
View Journal | View Issue

Cite this: *Nanoscale*, 2025, **17**, 25892

Particle size and shape effects on the magnetic behaviour of samarium hexacyanoferrate Prussian blue analogue

Nikolia Lalioti, *[a] Ntaniela Kalemai, [a] Ondrej Malina, [b,c] Radim Mach, [b] Zdeněk Baďura,[b,c] Alexandros N. Kalarakis [d] and Vassilis Tangoulis *[a]

We report the controlled synthesis of samarium–iron Prussian blue analogues (SmFe PBAs) with novel morphologies, achieved through a systematic reverse micelle strategy using the non-ionic surfactant Triton X-100. By varying key experimental parameters—such as the water-to-surfactant molar ratio (ω_0), the concentration of TX-100, and the volumetric ratio of cyclohexane to surfactant—we obtained a diverse range of particle shapes, including unprecedented daisy-like architectures with 4, 5, and 6 petals. These morphologies emerge within a narrow compositional window, implicating the formation of reverse bilayer vesicles as transient templates during nucleation and growth. Detailed morphological and structural characterization (TEM, SEM, XPS, PXRD, IR spectroscopy) revealed size-tunable particles ranging from 250 nm to 7 μm, while silica coating was achieved *via* a two-step sol–gel route enabling further miniaturization. Magnetic measurements highlight a strong size- and shape-dependent variation in coercive field (H_c), reaching up to 3320 Oe in submicron particles—among the highest reported for SmFe PBAs—attributed primarily to enhanced shape anisotropy. Our findings provide new insights into PBAs' morphology–property relationships and open pathways toward engineering anisotropic magnetic nanomaterials through soft templating in reverse micellar systems.

Received 26th August 2025,
Accepted 22nd October 2025

DOI: 10.1039/d5nr03619d

rsc.li/nanoscale

Introduction

The process of *morphosynthesis* in inorganic solids involves creating chemically based strategies to finely control the size, shape, and organization of materials across various length scales that extend beyond the unit cell.[1–3] This methodology is primarily inspired by the exploration of morphogenesis in natural biominerals, which frequently display unique crystal shapes at the nanoscale and exhibit remarkably intricate higher-order structures at the macroscopic scale.[3,4] Two leading strategies in morphosynthesis have emerged: utilizing biological and self-assembled organic supramolecular templates, as well as replicating structured reaction environments such as vesicles and microemulsions. These strategies have proven effective for traditional inorganic materials, including oxides, carbonates, and phosphates.[4,5]

Morphosynthesis in the form of microemulsion has enabled the production of nanoparticles, nanorods, thin films, and more complex architectures of molecular magnets derived from PBAs—historically the first coordination compound discovered serendipitously in Berlin 300 years ago in 1704.[6,7] This method relies on a unique dispersion system capable of dissolving both water-soluble and oil-soluble components due to its distinctive structure. The fundamental principle behind the microemulsion method involves combining the oil phase, water phase, and surfactant to establish a stable microemulsion system. These microemulsion systems typically exhibit very small particle sizes and maintain stability at the nanoscale. During the synthesis of PB/PBAs, two different types of microemulsions are usually mixed and stirred to achieve the desired product.[8–10] The microemulsion method is particularly prominent in the synthesis of PB nanoparticles for medical photothermal therapy.[11–13] PB nanoparticles possess strong near-infrared absorption properties, with their photothermal conversion mechanism based on energy level transitions and high photothermal stability.[14] For instance, Pang *et al.* employed a water-in-oil microemulsion method to prepare PB nanoparticles, demonstrating that the resulting

[a]*University of Patras, Department of Chemistry, Laboratory of Inorganic Chemistry, 26504 Patras, Greece. E-mail: lali@upatras.gr, vtango@upatras.gr*
[b]*Regional Centre of Advanced Technologies and Materials, Czech Advanced Technology and Research Institute, Palacky University, Slechtitelu 27, 77900 Olomouc, Czech Republic*
[c]*Nanotechnology Centre, Centre for Energy and Environmental Technologies, VSB-Technical University of Ostrava, 17. listopadu 2172/15, Ostrava-Poruba, Czech Republic*
[d]*Department of Mechanical Engineering, University of the Peloponnese, 26334 Patras, Greece*

material has potential applications in the post-treatment of tumors.[15]

One of the key advantages of synthesizing PB/PBAs through the microemulsion method is its ability to precisely control the morphology and size of the nanomaterials. The exchange of reactants among various water droplets facilitates rapid nucleation and the formation of surfactant-stabilized coordination complex nanoparticles. Moreover, the stable microcavities within microemulsions serve as nanoscale reactors, effectively limiting the nucleation, growth, and agglomeration of nanoparticles.[15] For instance, Tao *et al.* recently synthesized cubic-shaped Mn-PBA nanoparticles using a water-in-oil microemulsion.[16] The concentration of reactants and the ratio of water to surfactant are critical factors influencing the particle size of the PB/PBAs synthesized *via* this method. Vaucher *et al.* demonstrated that increasing the concentration of the reactant in the synthesis of cobalt hexacyanoferrate nanoparticles could lead to a reduction in nanoparticle size, which they attributed to the nucleation control principle.[17]

This pattern was observed during the synthesis of CoFe–PBAs, where the diameter of the "water droplets" within the microemulsion influenced the particle size.[18] It was found that increasing the reactant concentration from 0.006 mol L^{-1} to 0.009 mol L^{-1} resulted in the formation of hollow nanoparticles. However, when the reactant concentration was raised further to 0.100 mol L^{-1}, the product reverted to solid nanoparticles. Recently, Mansas *et al.* identified that varying the molar ratio of water to surfactant, ω_0, where the surfactant refers to [CuAOT], had a discernible impact on the size of the synthesized CuPBA nanoparticles.[19] At low values of ω_0, the nanoparticles' size correlated with that of the reverse micelles. As the values of ω_0 increased, the system approached instability, leading to a sudden increase in nanoparticle size and a broader distribution. Overall, the unified principles for controlling morphology are still under investigation.

The reverse-phase microemulsion method, derived from the original microemulsion technique, remains a prevalent approach for synthesizing poly (butyl acrylate) (PB)/poly (butyl acrylate) (PBA) nanoparticles. The benefit of this method lies in the ability to utilize water droplets within the surfactant monolayer as a tunable nanoreactor for the synthesis of target products with controlled sizes.[20] By employing sodium bis (2-ethylhexyl) sulfosuccinate (AOT) alongside polyvinylpyrrolidone (PVP) for protection, PB composite materials were successfully fabricated using a reversible microemulsion technique. They achieved average particle sizes of 20 nm, 23 nm, and 27 nm, corresponding to reactant ratios (w) of 10, 15, and 20, respectively.[21] This result strongly supports the aforementioned statement that controlling the size of w enables precise regulation of the particle size of PB/PBAs.

The synthesis of PBAs, where one of the metal ions is a trivalent lanthanide, especially in the case of $SmFe(CN)_6{\cdot}4H_2O$, produces various morphologies of the compound depending on the preparation method used. Using a reverse micelle system with polyoxyethylene (5) nonylphenyl ether (NP-5) in cyclohexane and water, nanorods were created with diameters ranging from 75 to 150 nm and aspect ratios of approximately 20 to 30.[22] In this method, the reaction occurred within aqueous nanodroplets of NP-5 reverse micelles, where crystal nucleation was confined to the nanoreactors. The interfacial surfactant film had a significant impact on crystal growth. The final formation of high-aspect-ratio, single-crystalline nanorods likely resulted from the oriented aggregation of primary nanoparticles.

In contrast, when a cetyltrimethylammonium bromide (CTAB) reverse micelle system was employed, nanobelts were produced with lengths of several tens of micrometers, widths of approximately 300 nm, and thicknesses of less than 20 nm. If a cosurfactant with a longer carbon chain replaced *n*-hexanol, the widths of the $SmFe(CN)_6{\cdot}4H_2O$ nanobelts decreased significantly. For instance, substituting *n*-decanol for *n*-hexanol resulted in nanobelts with widths of approximately 40 nm. The exact formation mechanism of the belt-like structure is still unclear. However, it is speculated that the cationic surfactant CTAB, aided by *n*-hexanol as a cosurfactant, interacts specifically with the {001} faces of $SmFe(CN)_6{\cdot}4H_2O$ crystals. This interaction likely restricts crystal growth along the [001] direction, resulting in the formation of $SmFe(CN)_6{\cdot}4H_2O$ nanobelts that have their *c*-axis aligned with the thickness direction.

Some years later, a novel synthesis method was developed for creating nanometric lanthanide hexacyanoferrate (Fe-CN-Ln) within a water/alcohol solution.[23] The resulting morphology of Fe-CN-Ln varied significantly depending on the specific lanthanide (Ln) used, producing structures that could be identified as hexagonal, asterisk-shaped, or rod-shaped, which contain acetic acid. Remarkably, the asterisk morphology was achieved with an impressive selectivity of over 80% by incorporating samarium (Sm). A new formation mechanism has been suggested in which alkylammonium cations, like ethylammonium (Et_4N^+), serve primarily as surface-active agents. Rather than functioning as ions that adsorb to surfaces to direct crystal growth on particular facets, they create soft nano-templates in the solution that facilitate the arrangement of Fe-CN-Sm nanocrystals into the desired asterisk morphology.

Inspired by the versatility of the reverse micelle method in producing different morphologies of SmFe PBAs, we decided to investigate the role of a non-ionic surfactant such as Triton X-100 (TX100) and optimize their magnetic properties by controlling the experimental conditions.

Experimental section

Materials

All manipulations were performed under aerobic conditions using reagents and solvents (Alfa Aesar, Sigma Aldrich, Acros Organics, Serva) as received. Samarium(III) chloride hexahydrate ($SmCl_3{\cdot}6H_2O$ 98%), iron(III) hexacyanoferrate ($K_3Fe(CN)_6$ 98%), (3-aminopropyl)triethoxysilane (APTES, $C_9H_{23}NO_3Si$ 98%) and Tetraethoxysilane (TEOS, $C_8H_{20}O_4Si$

98%) were purchased from Alfa Aesar. Anhydrous cyclohexane 99.5%, ethanol 100%, and acetone 99% were purchased from Sigma-Aldrich. Extra dry *n*-hexanol 99% was obtained from Acros Organics, and Triton X-100 was obtained from Serva.

General synthetic protocols for the preparation of SmFe PBAs

Nanoparticles of the SmFe PBAs were synthesized using the reverse micelle method under ambient conditions. Various synthetic parameters were studied, including (a) modification of the ω_0 parameter by changing the amounts of TX100 and *n*-hexanol in the oil phase while keeping the water amount constant; (b) the influence of hydrolysis and condensation of tetraethoxysilane (TEOS) and (3-aminopropyl)triethoxysilane (APTES); and (c) the role of NH_3 as a size-controlling agent. In particular, we investigated the effect of introducing TEOS into either the water or oil phases, as well as the impact of multi-stage addition of TEOS. Below, we will present the general experimental protocols for synthesizing Prussian blue analogs and their subsequent coating with silica (Scheme 1 and Table 1).

Protocol 1. An aqueous solution **A** containing the Sm(III) salt, $SmCl_3{\cdot}6H_2O$, is added dropwise under vigorous stirring using a micropipette to an organic mixture composed of the surfactant TX-100, the cosurfactant *n*-hexanol, and the solvent cyclohexane. The resulting colorless solution **A** is stirred at room temperature for 3 minutes until a water-in-oil microemulsion **A′** forms. A similar procedure is then carried out with a second aqueous yellow solution **B** containing $K_3Fe(CN)_6$, leading to the formation of a water-in-oil microemulsion **B′**. Microemulsion **A′** is then rapidly combined with microemulsion **B′** under vigorous stirring at room temperature, resulting in a bright orange one. This mixture is incubated for 24 hours at 50 °C. The reaction is terminated by adding acetone, which causes the precipitation of nanoparticles (NPs). The NPs are isolated after being washed successively with ethanol (three washes of 13 mL each) and acetone (one wash of 13 mL), followed by centrifugation for 30 minutes at 6000 rpm. Finally, the NPs are dried overnight in an oven set to 50 °C.

Protocol 2. Modification of Protocol 1 with the addition of NH_3 after the mixing of microemulsions A′ and B′.

Protocol 3. This modification of Protocol 1 introduces a two-step sol–gel method, with the first step involving the addition of TEOS to aqueous solutions A and B (TEOS_W). The second step starts 24 hours after mixing the two microemulsions, **A′** and **B′**. First, APTES is introduced, followed 30 minutes later by TEOS, into the orange microemulsion while stirring vigorously at room temperature. The resulting bright orange microemulsion is then stirred for an additional 24 hours at room temperature, resulting in a total stirring time of 48 hours.

Table 1 Experimental conditions for the SmFe PBAs

SmFe NPs	Protocol	Cyclohexane/*n*-hexanol/TX100[a]	ω_0	[TX100][b]	Size controlling agents
NP1	P1	7.5/0.9/0.9	9	0.20	—
NP2	P1	7.5/1.8/1.8	4.5	0.40	—
NP3	P1	7.5/3.8/3.8	2	0.84	—
NP4	P1	3.6/0.9/0.9	9	0.40	—
NP5	P2	7.5/1/8/1.8	4.5	0.40	NH_3
NP6	P3	7.5/1.8/1.8	4.5	0.40	APTES/TEOS

[a] Volumetric ratio. [b] Concentrations (*M*) (volumetric ratio to cyclohexane).

Synthesis of SmFe PBAs

NP1. The material was prepared following the synthetic procedure as described in Protocol 1. The aqueous solution A contains 0.25 mL H_2O and $SmCl_3{\cdot}6H_2O$ (0.5 mmol), and the aqueous solution B contains 0.25 mL H_2O and $K_3Fe(CN)_6$ (0.2 mmol). Each organic phase, to which aqueous solutions A and B will be added, contains 7.5 mL cyclohexane, 0.9 mL *n*-hexanol, 0.9 mL Triton X-100 (Table 1). The final product was collected *via* filtration. IR bands (KBr, cm^{-1}): 3615(m), 3527(w), 3384(m), 3256(w), 2147(s), 2136(s), 2106(w), 2095(w), 2060(w), 1677(w), 1632(m), 1608(m), 693(m), 418(w).

NP2. The material was prepared following the synthetic procedure as described in Protocol 1. The aqueous solution A contains 0.25 mL H_2O and $SmCl_3{\cdot}6H_2O$ (0.5 mmol), and the aqueous solution B contains 0.25 mL H_2O and $K_3Fe(CN)_6$ (0.2 mmol). Each organic phase contains 7.5 mL of cyclohexane, 1.8 mL of *n*-hexanol, and 1.8 mL of TX-100 (Table 1). IR bands (KBr, cm^{-1}): 3615(m), 3527(w), 3384(m), 3256(w), 2147(s), 2136(s), 2106(w), 2095(w), 2060(w), 1677(w), 1632(m), 1608(m), 693(m), 418(w).

NP3. The material was prepared following the synthetic procedure as described in Protocol 1. The aqueous solution A contains 0.25 mL H_2O and $SmCl_3{\cdot}6H_2O$ (0.5 mmol), and the aqueous solution B contains 0.25 mL H_2O and $K_3Fe(CN)_6$ (0.2 mmol). Each organic phase contains 7.5 mL of cyclohexane, 3.6 mL of *n*-hexanol, and 3.6 mL of TX-100 (Table 1).

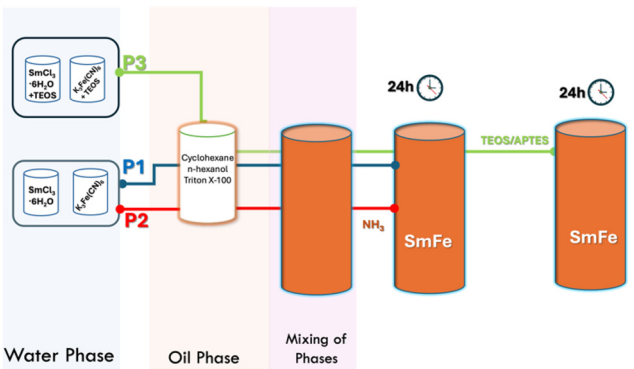

Scheme 1 The experimental protocols P1, P2, and P3 are illustrated schematically, with P1 depicted in navy blue, P2 in red, and P3 in green. The duration of protocols P1 and P2 was 24 hours, while protocol P3 lasted for 48 hours. The experimental protocols P1–P3 depicted in different colours: P1 (blue navy); P2 (red); P3 (green). The ending of protocols P1 and P2 occurred after 24 hours, while for protocol P3, the duration was 48 hours.

IR bands (KBr, cm^{-1}): 3613(m), 3531(w), 3384(mb), 3261(w), 2148(s), 2136(s), 2107(w), 2096(w), 2065(m), 1951(w), 1678(w), 1633(m), 1608(m), 1403(w), 1100(w), 692(m), 580(w), 422(w), 416(w).

NP4. The material was prepared following the synthetic procedure as described in Protocol 1. The aqueous solution A contains 0.25 mL H_2O and $SmCl_3{\cdot}6H_2O$ (0.5 mmol), and the aqueous solution B contains 0.25 mL H_2O and $K_3Fe(CN)_6$ (0.2 mmol). Each organic phase contains 3.6 mL of cyclohexane, 0.9 mL of *n*-hexanol, and 0.9 mL of TX-100 (Table 1). IR bands (KBr, cm^{-1}): 3613(m), 3531(w), 3380(mb), 3261(m), 2148(s), 2136(s), 2106(w), 2096(w), 2063(m), 1950(w), 1679(w), 1633(m), 1608(m), 688(m), 422(w), 412(w).

NP5. The material was prepared following the synthetic procedure as described in Protocol 2. The aqueous solution A contains 0.25 mL H_2O and $SmCl_3{\cdot}6H_2O$ (0.5 mmol). The aqueous solution B contains 0.25 mL H_2O and $K_3Fe(CN)_6$ (0.2 mmol). Each organic phase contains 7.5 mL of cyclohexane, 1.8 mL of *n*-hexanol, and 1.8 mL of TX-100. 15 minutes after the mixing of microemulsions A′ and B′, 0.124 mL NH_3 is added to the orange microemulsion (Table 1). This is followed by stirring for 24 hours at room temperature, after which the final product is collected. IR bands (KBr, cm^{-1}): 3613(m), 3529(w), 3382(wb), 3261(w), 2148(s), 2136(s), 2105(w), 2095(w), 2061(m), 1954(w), 1677(w), 1633(m), 1608(m), 1403(w), 1070(w), 951(w), 695(m), 584(w), 418(w).

NP6. The material was prepared following the synthetic procedure as described in Protocol 3. The aqueous solution A contains 0.25 mL H_2O, $SmCl_3{\cdot}6H_2O$ (0.5 mmol), and 0.1 mL TEOS. The aqueous solution B contains 0.25 mL H_2O, $K_3Fe(CN)_6$ (0.2 mmol), and 0.1 mL TEOS. Each organic phase contains 7.5 mL of cyclohexane, 1.8 mL of *n*-hexanol, and 1.8 mL of Triton X-100. 24 hours after mixing the two microemulsions, 0.1 mL APTES was added, followed by 0.1 mL TEOS 30 minutes later, to the microemulsion under vigorous stirring (Table 1). IR bands (KBr, cm^{-1}): 3613(w), 3397(b), 3259(w), 3382(wb), 2898(m), 2811(w), 2711(w), 2618(w), 2537(w), 2435(w), 2366(w), 2311(w), 2240(w), 2148(s), 2136(s), 2106(w), 2096(w), 2061(m), 1951(w), 1677(w), 1633(w), 1608(m), 1492(m), 1411(w), 1332(w), 1224(w), 1133(s), 902(m), 692(m), 602(w), 586(w), 574(w), 534(w), 472(w), 464(w), 443(w), 435(w), 428(w), 420(w), 412(w), 408(w).

Results and discussion

Synthetic comments

The reverse aggregation behaviour of TX-100 in cyclohexane is well-established, supported by various measurements, including conductivity, light scattering, and a range of spectroscopic techniques such as NMR, FT-IR, and UV–vis absorption and emission studies using different probes.[24–36] Typically, alcohol is incorporated as a co-surfactant to facilitate the formation of aggregates such as reverse micelles and lamellar structures. TX-100 is a non-ionic surfactant, comprising an aromatic group linked to a nonpolar alkyl chain, along with around 9.5 ethylene oxide (EO) units that form the polar segment, capped with a hydroxyl group. The poly(ethylene oxide) (PEO) blocks act as hydrogen bond acceptors and can form complexes with cations.[36–38] Consequently, TX-100 aggregates can solubilize substantial amounts of water within nonpolar environments. Drawing on this understanding, reverse aggregates of TX-100 in a mixture of *n*-hexanol, cyclohexane, and water at varying compositions have been detailed and employed to generate a variety of structures (Fig. S1).[39–42]

The synthesis of the first three (3) SmFe PBAs (**NP1–NP3**) followed the experimental protocol P1 with ratios of w_0 equal to 9, 4.5, and 2 while keeping the water concentration at a very low content. According to this protocol, microemulsions were created by mixing the water phases of the coordination complex reagents with the organic phase of cyclohexane, containing TX100 and the co-surfactant *n*-hexanol, for a total stirring time of 24 hours. The morphology of the final SmFe PBAs (**NP1**) for the case of ω_0 = 9 can be described as asterisks in the microscale based on TEM microscopy (Fig. 1 and Fig. S1) with dimensions close to 7.0 μm. Quite surprisingly, this finding contradicts the literature reports where (a) the asterisk morphology is related to a mechanism where a cationic surfactant functions as a soft template that facilitates the asterisk arrangement of Fe-CN-Sm nanocrystals[23] and (b) the nanorod morphology is documented with the application of a non-ionic surfactant.[22] By keeping ω_0 fixed to 9 and increasing the volume of the organic phase two times (15 ml of cyclohexane), SmFe PBAs were produced with similar morphology and average sizes.

Reducing the value of ω_0 to 4.5, an anisotropic growth of SmFe PBAs (**NP2**) has been monitored for the first time (Fig. 1 and Fig. S3–S7), with morphologies that can be described as 6, 5, and 4-petal daisy-like structures, featuring an interesting hollow structure for the case of 6 petals. The size and percentage of different shapes of the particles were determined by "manual counting" (Fig. S1) using a methodology described in SI (Fig. S8). The average particle size ranges from 0.9 to

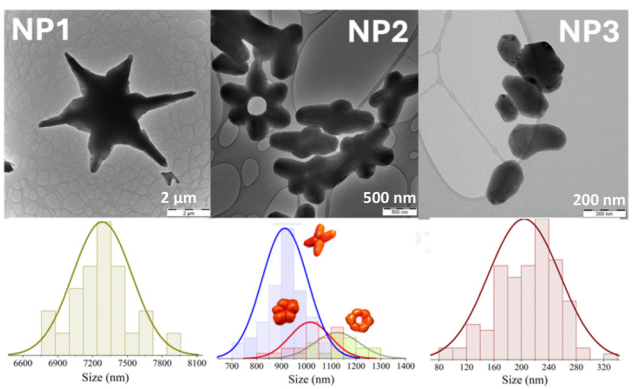

Fig. 1 TEM images of **NP1**, **NP2** and **NP3** and the distributions of their sizes. For the case of **NP2** the distribution of sizes for the three different morphologies is presented. The relative heights of the Gaussian distributions are based on the percentage of each type (see text for details).

1.1 μm, while the percentage of each type is 18%, 22%, and 60% for the 6, 5, and 4-petal daisy-like morphologies, respectively. It should be noted that these morphologies are being documented for the first time, as the reported shapes to date have been either asterisks or nanorods, nanowires, or nanobelts.[22,23] For $\omega_0 = 2$, a further size reduction is monitored with SmFe PBAs (**NP3**), having an average size of 250 nm and an undefined morphology (Fig. 1 and Fig. S9). All synthetic efforts for $\omega_0 < 2$ resulted in instability issues, including the breakdown of micelle structure and the formation of larger, less uniform aggregated particles.

To further investigate the growth mechanism of the SmFe PBAs and the evolution of these new morphologies, synthetic efforts were focused on $\omega_0 = 4.5$ while varying other synthetic parameters. Initially, by reducing the organic phase to half (3.8 mL), similar morphologies of SmFe PBAs (**NP4**) were observed (Fig. 2 and Fig. S10), with an overall size reduction to a value of 0.6–0.8 μm. At the same time, the percentage of each type has been adjusted to 25%, 45%, and 30% for the 6-, 5-, and 4-petal daisy-like morphologies, respectively.

The influence of NH_3 as a size-controlling agent is examined in the synthesis of SmFe PBAs by keeping $\omega_0 = 4.5$ and adding NH_3 after mixing the microemulsions. The morphology of the final SmFe PBAs (**NP5**) retained the daisy-like four petals structure, but the sizes were reduced to an average value of 300 nm (Fig. 2 and Fig. S11). No hollow structures were observed. To provide an effective SiO_2 coating to the SmFe PBAs and examine its size-controlling effect, several synthetic approaches have been employed (see SI); however, only two have proven successful, yielding similar results regarding the size of the PBAs and their overall morphology (Fig. 2 and Fig. S12–S14). One of these methodologies utilizes a two-step approach, involving the hydrolysis and condensation of TEOS/APTES, based on our group's established protocol for silica coating of spin-crossover nanoparticles.[43] According to this method, TEOS is added to the water phase (1st stage), while TEOS/APTES is added 24 hours after mixing the microemulsions (2nd stage). Following this protocol, silica-covered SmFe PBAs (**NP6**) were produced, resulting in a reduction in size to 200 nm with a daisy-like four-petal structure. The silica does not homogenously cover the surface of the PBAs, which are heavily aggregated (Fig. 2 and Fig. S12).

A detailed analysis of the formation of these new morphologies implicates a theoretical investigation, which is beyond the scope of this paper. We believe that several factors influence the daisy-like structure of the SmFe PBAs: (a) the volume ratio of cyclohexane to TX100, (b) the concentration of TX100, and (c) the very low water content. Under these conditions, there is insufficient aqueous phase to enable the surfactant to form reverse micelles that can effectively disperse in the oil phase. The high concentration of TX100 (>0.2 M) enables oil to infiltrate the polar core of the micelles, facilitating the formation of reverse bilayer vesicles of TX100. HRTEM/SEM images reveal that the daisy-like morphology comprises a polycrystalline structure composed of SmFe nanocrystals. This formation occurs due to the assembly of a "necklace" of rod-shaped SmFe nanocrystals within the reverse bilayer vesicles, as confirmed by the presence of incomplete fragments observed in SEM and HRTEM images (Fig. 3). At low concentrations of TX100 (<0.2 M) within a cyclohexane/hexanol system, the lipophilic aromatic hydrocarbon regions of the surfactant TX100 organize effectively at the oil–water interface,

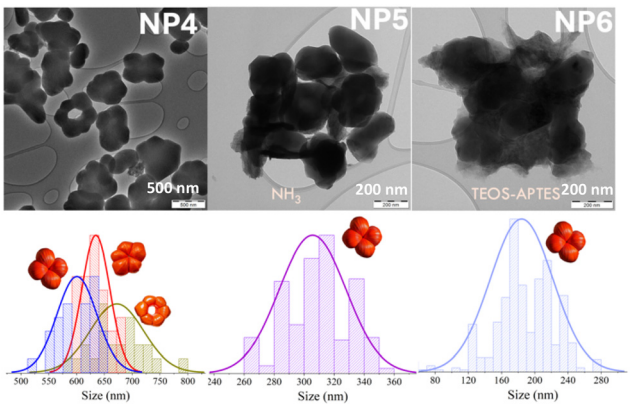

Fig. 2 TEM images of **NP4**, **NP5** and **NP6** and the distributions of their sizes. For the case of **NP4** the distribution of sizes for the three different morphologies is presented. The relative heights of the Gaussian distributions are based on the percentage of each type (see text for details).

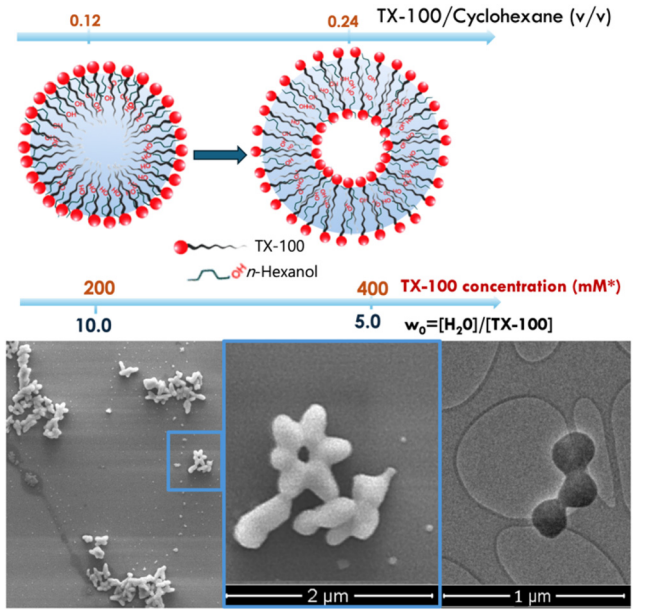

Fig. 3 (A) Proposed mechanism for the formation of daisy-like SmFe PBAs. For concentrations of TX100 > 0.2 M or volumetric ratio of TX100/cyclohexane > 0.24 a transition occurs from a single to a double reverse bilayer vesicle. The water phase is shown in blue while the *n*-hexanol is added as a co-surfactant to facilitate the formation process (see text for details). (B) and (B1). SEM image of **NP2** displaying incomplete fragments of a "necklace" of rod-shaped SmFe nanocrystals near a daisy-like particle (highlighted within the blue rectangle). (C). TEM image of **NP2** illustrating an incomplete fragment of a "necklace" of rod-shaped SmFe nanocrystals.

whereas, at the same time, the hydrophilic tails penetrate the hexanol/water droplets, leading to the formation of solid nanoparticles.

The filling of the hollow structures and their transition to solid polycrystalline morphologies resembling 6, 5, or 4 daisies, as well as the distribution of these morphologies observed in the reverse micelle experiment, will be addressed in a future investigation.

Interestingly, a recent publication highlights the role of reverse bilayer vesicles in the formation of hollow silica nanoparticles. According to Wu *et al.*,[44] who introduced a reverse micellar strategy for synthesizing SiO_2 NPs using a system of cyclohexane/TX100/octanol, it is feasible to create TX100 reverse bilayer vesicles when the volume ratio of cyclohexane to TX100 is less than 7.0, and the concentration of TX100 is greater than 0.2 M (in volumetric ration to cyclohexane). This type of vesicle plays a crucial role in forming the hollow SiO_2 NPs. Conversely, when the concentration of TX100 is below the threshold of 200 mM, micelle monolayer structures of TX100 form, leading to the production of solid SiO_2 NPs.

Structural characterization of SmFe PBAs

The FT-IR spectrum of SmFe PBA nanoparticles (Fig. 4) initially shows a sharp peak at 3615 cm^{-1}, which is due to ν(O–H) stretching vibrations of water molecules located in the unit cell without forming hydrogen bonds. The spectrum then shows a medium peak at 3528 cm^{-1}, a strong peak at 3384 cm^{-1} (with a shoulder at 3409 cm^{-1}), and a sharp peak at 3256 cm^{-1}. These are due to ν(O–H) stretching vibrations of water molecules involved in a hydrogen-bonded network. Then, the strong peaks at 2147 cm^{-1} and 2136 cm^{-1} are attributed to stretching vibrations ν(C≡N) of the bridging cyano-ligands (Fe(III)–C≡N–Sm(III)). One possible reason for the existence of two distinct CN peaks is the bonding environment of the CN groups. There are two distinct C–N bond distances, which vary slightly across the lanthanide series. This variation is thought to result from subtle differences in back-donation effects and electrostatic interactions.[45] These differences arise due to electronic effects, specifically back-donation from Fe(III) into the CN antibonding π-orbitals, which subtly alter CN bond lengths and their stretching frequencies. One of the C–N bonds tends to shorten due to stronger electrostatic interactions, while the other one has a higher electronic population, leading to longer CN bonds. In contrast, the weak peaks at 2106 cm^{-1} and 2096 cm^{-1} are related to $^{12}C^{15}N$ and $^{13}C^{14}N$ stretching bands, respectively.[45] The medium peak at 2060 cm^{-1}, is attributed to stretching vibrations ν(C≡N) of the terminal cyano-ligands.[45,46] It should be noted that the same number of bands discussed above have been observed in bulk lanthanide PBAs synthesized using micro synthetic methods[45] as well as nanoparticles.[47] Then, the sharp peaks at 1632 cm^{-1} and 1608 cm^{-1} are due to δ(H–O–H) bending vibrations of water molecules. Finally, the peaks at 693 cm^{-1} and 419 cm^{-1} are attributed to δ(Fe–C–N) bending vibrations and ν(Fe–C) stretching vibrations of the FeC_6 octahedra, respectively.[47] For the case of silica covered **NP6** the additional vibrations of Si–O–Si at 1090 cm^{-1} and 798 cm^{-1} are observed as well as peaks denoted with an asterisk that belong to impurities of TX-100.

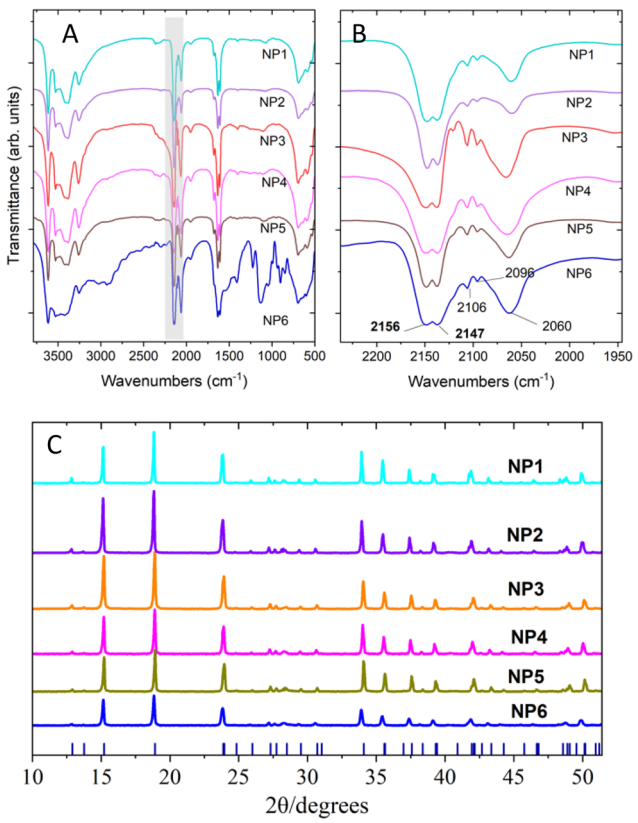

Fig. 4 (A) FT-IR spectra of **NP1–NP6** where the grey area reveals the vibrations of the bridging and terminal cyano-ligands. (B) Highlight of the grey area. (C) PXRD diffraction patterns of **NP1–NP6**.

P-XRD studies and Rietveld analysis revealed the crystallinity of the SmFe NPs with an orthorhombic structure[48] (JCPDS no. 84-1954) while the metal ratio, Sm/Fe, was close to 1.0 based on EDS and XPS measurements (Fig. S15 and S16). The calculated lattice parameters of the SmFe NPs are presented in Table S1 while elemental analysis and estimated molecular formulas are given in Table S2.

Magnetic properties of SmFe NPs

The temperature dependence of the susceptibility data in the form of $\chi_M T$ *vs.* T for all the SmFe PBAs is shown in Fig. 5 and Fig. S17. The $\chi_M T$ value at room temperature is in the range 0.54–0.60 emu mol^{-1} K (μ_{eff} = 2.1–2.2μ_B), close to the value expected for an uncoupled system of a low spin ion of Fe(III) with μ_{eff} = 2.54μ_B and a Sm(III) ion with μ_{eff} value close to 0.8μ_B, resulting in an overall $\mu_{calc.} = \sqrt{\mu_{Fe}{}^2 + \mu_{Sm}{}^2} = 2.65\mu_B$ or $\chi_M T_{calc.}$ = 0.877 emu mol^{-1} K. The onset of a 3D ferrimagnetic ordering of the system is confirmed by a minimum in the $\chi_M T$ curves at 10–15 K accompanied by a drastic increase of the susceptibility upon further cooling to values close to 7.3–8.9 emu mol^{-1} K for **NP1–NP5** and 4.2 emu mol^{-1} K for **NP6** at 3 K. Further decrease of the temperature leads to saturation of the susceptibility values.

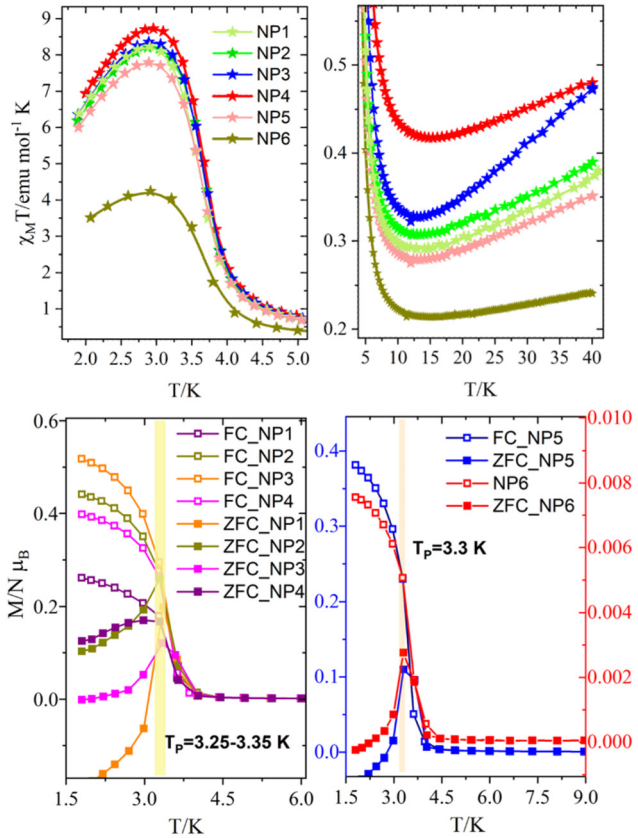

Fig. 5 (upper) Temperature dependence of the susceptibility data in the form of $\chi_M T$ and in the temperature range 2–5 K (left) and 4–45 K (right). (lower) ZFC-FC measurements at 100 Oe for the **NP1–NP4** (left) and **NP5–NP6** (right).

The inverse susceptibility data, which are shown in Fig. S18, further confirmed the ferrimagnetic ordering. The Curie–Weiss law, $\chi_M = C/(T - \theta)$, is applied for temperatures above 100 K and is shown as a solid line in the same Figure. The results of the fitting procedure are presented in Table S3, where the value of the constant C is close to 0.65 emu mol^{-1} K, corresponding to a room-temperature effective magnetic moment $\mu_{eff} = 2.30\mu_B$. The paramagnetic Curie temperature, θ, is negative in the range of −60 to −95 K due to the convex nature of the curve, denoting the antiferromagnetic interaction between the magnetic centers. It should be noted that the calculated θ value for the bulk system is −68 K.[49] The deviation from the Curie–Weiss law for temperatures lower than 100 K is related to the crystal field effect of the lanthanide. A significant change in the slope of the curves for temperatures below 4 K confirms the onset of magnetic ordering.

The T_C value of the SmFe PBAs was investigated using ZFC-FC measurements performed at a small external field of 100 Oe, and the results are shown in Fig. 5. The differences between the two curves are evident below 4 K, where the ZFC curves reveal a peak with a maximum centred in the range T_C = 3.25–3.35 K. It should be noted here that for the case of **NP1**, **NP5** and **NP6** negative magnetization was observed which may arise from an unpropped zero-field cooling process. Additionally, the instrument's residual magnetic field may exhibit negative values, which could induce corresponding negative magnetization at low temperatures.[50]

The magnetization curves of SmFe PBAs at 2 K are shown in Fig. 6 and Fig. S19 in the form of reduced magnetization ($M/N\mu_B$) *vs.* external field H. Magnetization does not saturate at an external field of 5 T. The saturated values have been calculated by an extrapolation from the $M(1/H^2)$ plots at 2 K, which are shown in Fig. S20. The saturation values are shown in Table S2 and are close to 0.7–0.8μ_B for **NP1–NP4**, **NP6**, and 0.5μ_B for **NP5**. It should be noted that the theoretical saturation value is $M_s = g_{Fe}J_{Fe} - g_{Sm}J_{Sm} = (1.732–0.714)\mu_B = 1.01\mu_B$.

Quite interestingly, a shape/size dependence of the coercive field (H_c) is monitored according to which the coercivity increases from 503 Oe for the case of **NP1** (microstars, close to the bulk case) to 2330 Oe for **NP2** (6, 5, and 4-petal daisy-like structures with an average size 0.9–1.1 μm) and reaches the highest ever observed value of 3320 Oe for the **NP3** (undefined morphology with an average size 250 nm). The H_c values for the rest of the SmFe PBAs are 1940 Oe (**NP4**), 2120 Oe (**NP5**), and 2200 Oe for **NP6**. An analogous shape/size dependence of H_c has been observed for the case of SmFe rods, where H_c increased from a value of 785 Oe (microrods) to 2765 Oe (nanorods).

A possible explanation for this increase can be provided, considering that the coercivity is related to the properties of spin carriers and the geometry of the PBAs. An increase in coercivity is associated with enhanced magnetic anisotropy, indicating that an externally applied magnetic field at a specific temperature can effectively overcome the energy barrier required to change the direction of magnetization. The enhancement of magnetic anisotropy in SmFe PBAs, which is the sum of bulk magneto-crystalline anisotropy and shape anisotropy, is primarily related to the shape anisotropy part, as this contribution promotes the alignment of magnetization along the principal axis of the material, significantly influen-

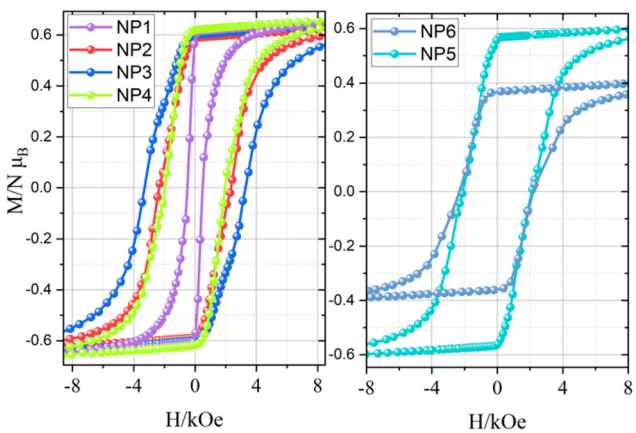

Fig. 6 Field dependence of the reduced magnetization, $M/N_{\mu B}$ for the **NP1–NP4** (left) and **NP5–NP6** (right) at 2 K and in the range −8 kOe to 8 kOe.

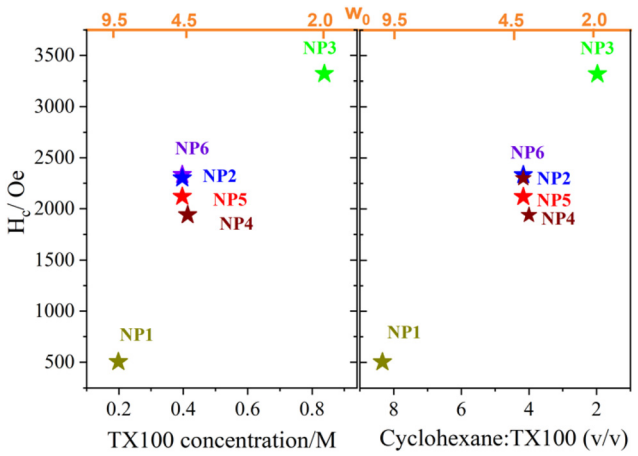

Fig. 7 Dependence of H_c on (left) the concentration of TX100 and (right) the volumetric ratio of cyclohexane to TX100. In both plots, the dependence of the ratio ω_0 on the above-mentioned parameters is shown in orange colour.

cing the magnitude of the coercive field. Unfortunately, it is not possible to calculate the shape anisotropy constant from the equation $K = NM_s^2/2$ since the demagnetization factor N is not defined for such complex morphologies.

To illustrate the correlation between the key experimental parameters of this study and the magnetic behaviour of the synthesized SmFe PBAs, two plots have been created and are shown in Fig. 7. The first plot shows the dependence of H_c on the volumetric ratio of cyclohexane to TX100, while the second plot displays the relationship between H_c and the concentration of TX100. In both plots, the dependence of the ratio ω_0 on the aforementioned parameters is also presented. A direct observation from the plots indicates that the magnetic anisotropy, as measured by the value of H_c for the particles, increases when the value of ω_0 approaches its lower limit (approximately 2.0). This value is also associated with the highest concentration of TX100 (0.8 M) or the lowest volumetric ratio of cyclohexane to TX100 (around 2.0). Daisy-like morphologies have been observed for ω_0 values of 4.5 and concentrations of TX100 exceeding the threshold of 0.2 M (but remaining below 0.8 M). Although the synthesized PBAs, identified as **NP2**, **NP4**, **NP5**, and **NP6**, vary in size and morphology, the value of H_c shows only minor variations, ranging from 1940 to 2330 Oe. The least anisotropic behaviour, represented by H_c = 503 Oe, was recorded for the highest ω_0 value of 9.5, which corresponds to PBAs exhibiting asterisk morphology (**NP1**). Synthetically, these particles are linked to TX100 concentrations near 2.0 or a volumetric ratio of cyclohexane to TX100 close to 0.8 M.

Conclusions

We reported the synthesis of SmFe PBAs using reverse micelle methods, highlighting the ability to control their morphology and size through variations in key experimental parameters. By adjusting the volumetric ratio of cyclohexane to TX100, the concentration of TX100, and the water content, unique morphologies such as asterisks and daisy-like structures (4, 5, and 6 petals), were achieved. Notably, the daisy-like structures were documented for the first time, marking a significant advancement in the field of morphosynthesis.

The study reveals that the water-to-surfactant molar ratio (ω_0) and TX100 concentration play critical roles in determining the size and shape of SmFe PBAs.Lower ω_0 values (approximately 2) and higher TX100 concentrations (above 0.2 M) promote the formation of smaller particles, while higher ω_0 values (around 9) result in larger particles. These findings underscore the importance of precise control over experimental conditions to tailor nanoparticle properties.

A clear correlation has been established between the sizes of SmFe PBAs and their magnetic properties, particularly the coercive field (H_c), revealing how size and shape influence magnetic anisotropy. The smallest particles, with undefined morphologies and an average size of 250 nm (**NP3**), exhibited the highest coercive field (H_c) of 3320 Oe which is attributed to enhanced magnetic anisotropy. Particles with daisy-like structures (**NP2**, **NP4**, **NP5**, **NP6**) and sizes ranging from 300 nm to 1.1 μm demonstrated H_c values between 1940 Oe and 2330 Oe. These morphologies, featuring 4, 5, and 6 petals, exhibit moderate magnetic anisotropy due to their unique, anisotropic shapes. The largest particles, with asterisk-like morphologies (**NP1**) and sizes around 7 μm, showed the lowest H_c of 503 Oe. This reduced coercivity is linked to lower shape anisotropy, as the bulk-like morphology does not favor strong magnetic alignment. The onset of ferrimagnetic ordering is confirmed at low temperatures (below 4 K).

The introduction of novel morphologies, such as hollow daisy-like structures, and the proposed mechanisms for their formation represent a significant contribution to the field. Factors such as reverse bilayer vesicles, surfactant interactions, and the assembly of rod-shaped nanocrystals within vesicles are suggested to influence the observed morphologies. These findings open new avenues for exploring the growth mechanisms and optimizing synthetic strategies.

Future investigations will focus on understanding the theoretical aspects of the growth mechanisms, including the role of reverse bilayer vesicles in forming hollow structures. Additionally, the transition of hollow structures to solid polycrystalline morphologies and their distribution in reverse micelle experiments will be addressed. These studies aim to refine the synthesis process further and expand the applications of SmFe PBAs in various fields.

In conclusion, this work provides valuable insights into the synthesis, morphology control, and magnetic behavior of SmFe PBAs, introducing novel morphologies and highlighting the importance of experimental parameters in tailoring their properties. The findings pave the way for future research and potential applications in advanced materials and nanotechnology.

Author contributions

Conceptualization: N. L., V. T.; investigation: N. K., O. M., R. M., A. K., Z.B.; writing – original draft preparation: N. L., V. T.; writing – review and editing: N. L., V. T., O. M., and A. K. All authors have read and agreed to the published version of the manuscript.

Conflicts of interest

There are no conflicts to declare.

Data availability

The data supporting this article have been included as part of the supplementary information (SI). Supplementary information: experimental details, critical ratios for water/TX100/*n*-hexanol, TEM supplementary images, synthetic attempts for silica covering of SmFe PBAs, P-XRD analysis, EDS analysis, XPS analysis, magnetic study of $1/\chi_M$ curves and $M(1/H^2)$ plots. See DOI: https://doi.org/10.1039/d5nr03619d.

Acknowledgements

O. M. acknowledges the financial support of the European Union under REFRESH – Research Excellence for Region Sustainability and High-tech Industries (project no. CZ.10.03.01/00/22-003/0000048) and the Research Infrastructure NanoEnviCz, supported by the Ministry of Education, Youth, and Sports of the Czech Republic (project no. LM2023066).

References

1 E. Dujardin and S. Mann, *Adv. Mater.*, 2004, **16**, 1125–1129.
2 S. Mann, S. A. Davis, S. R. Hall, M. Li, K. H. Rhodes, W. Shenton, S. Vaucher and B. J. Zhang, *J. Chem. Soc., Dalton Trans.*, 2000, 3753–3763.
3 S. Mann, *Biomineralization. Principles and Concepts in Bioinorganic Materials Chemistry*, Oxford University Press, Oxford, UK, 2001.
4 E. Dujardin and S. Mann, *Adv. Mater.*, 2002, **14**, 775–788.
5 S. A. Davis, E. Dujardin and S. Mann, *Curr. Opin. Solid State Mater. Sci.*, 2003, **7**, 273–281.
6 Anonymous, *Miscellanea Berolinensia as incrementum scientiarum*,Berlin, 1710, p. 377.
7 J. Woodward, *Philos. Trans. R. Soc. London*, 1724, **XXXIII**, 15.
8 S. P. Moulik, G. C. De, A. K. Panda, B. B. Bhowmik and A. R. Das, *Langmuir*, 1999, **15**, 8361–8367.
9 M. F. Dumont, O. N. Risset, E. S. Knowles, T. Yamamoto, D. M. Pajerowski, M. W. Meisel and D. R. Talham, *Inorg. Chem.*, 2013, **52**, 4494–4501.
10 Y. Q. Lin, L. H. Zhang, Y. Xiong, T. Wei and Z. J. Fan, *Energy Environ. Mater.*, 2020, **3**, 323–345.
11 J. Li, X. M. Liu, L. Tan, Z. D. Cui, X. J. Yang, Y. Q. Liang, Z. Y. Li, S. L. Zhu, Y. F. Zheng, K. W. K. Yeung, X. B. Wang and S. L. Wu, *Nat. Commun.*, 2019, **10**, 4490.
12 J. Zhou, M. H. Li, Y. H. Hou, Z. Luo, Q. F. Chen, H. X. Cao, R. L. Huo, C. C. Xue, L. Sutrisno, L. Hao, Y. Cao, H. T. Ran, L. Lu, K. Li and K. Y. Cai, *ACS Nano*, 2018, **12**, 2858–2872.
13 W. S. Chen, K. Zeng, H. Liu, J. Ouyang, L. Q. Wang, Y. Liu, H. Wang, L. Deng and Y. N. Liu, *Adv. Funct. Mater.*, 2017, **27**, 1605795–1605804.
14 Y. J. Su, Y. Wang, Z. L. Lu, M. H. Tian, F. Wang, M. Y. Wang, X. A. Diao and X. L. Zhong, *Chem. Eng. J.*, 2023, **456**, 141075–141086.
15 H. J. Pang, C. Tian, G. H. He, D. Zhang, J. H. Yang, Q. B. Zhang and R. Y. Liu, *Nanoscale*, 2021, **13**, 8490–8497.
16 Q. Tao, G. H. He, S. Ye, D. Zhang, Z. D. Zhang, L. Qi and R. Y. Liu, *J. Nanobiotechnol.*, 2022, **20**, 18.
17 S. Vaucher, J. Fielden, M. Li, E. Dujardin and S. Mann, *Nano Lett.*, 2002, **2**, 225–229.
18 H. Liu, X. L. Du, C. H. Liang, P. Liu, J. F. Xu, J. A. Fang, W. G. Shen and J. H. Zhao, *Synth. React. Inorg., Met.-Org., Nano-Met. Chem.*, 2010, **40**, 805–811.
19 C. Mansas, C. Rey, X. Deschanels and J. Causse, *Colloids Surf., A*, 2021, **624**, 126772–126784.
20 F. X. Bu, C. J. Du, Q. H. Zhang and J. S. Jiang, *CrystEngComm*, 2014, **16**, 3113–3120.
21 Z. H. Li, J. L. Zhang, T. C. Mu, J. M. Du, Z. M. Liu, B. X. Han and J. Chen, *Colloids Surf., A*, 2004, **243**, 63–66.
22 H. L. Sun, H. T. Shi, F. Zhao, L. M. Qi and S. Gao, *Chem. Commun.*, 2005, 4339–4341.
23 M. Yamada and S. Yonekura, *J. Phys. Chem. C*, 2009, **113**, 21531–21537.
24 M. F. T. Reis, R. C. F. Bonomo, A. O. de Souza, L. H. M. da Silva, C. M. Veloso, L. A. Minim and R. D. I. Fontan, *Food Res. Int.*, 2012, **49**, 672–676.
25 T. Arai, A. Hashidzume and T. Sato, *Macromolecules*, 2015, **48**, 4055–4062.
26 M. E. Flores, F. Martínez, A. F. Olea, T. Shibue, N. Sugimura, H. Nishide and I. Moreno-Villoslada, *J. Phys. Chem. B*, 2015, **119**, 15929–15937.
27 L. M. Qi and J. M. Ma, *J. Colloid Interface Sci.*, 1998, **197**, 36–42.
28 C. Kumar and D. Balasubramanian, *J. Colloid Interface Sci.*, 1980, **74**, 64–70.
29 M. E. Flores, T. Shibue, N. Sugimura, H. Nishide, F. Martínez, A. F. Olea and I. Moreno-Villoslada, *J. Mol. Liq.*, 2014, **199**, 301–308.
30 C. Kumar and D. Balasubramanian, *J. Colloid Interface Sci.*, 1979, **69**, 271–279.
31 C. Kumar and D. Balasubramanian, *J. Phys. Chem.*, 1980, **84**, 1895–1899.
32 A. Kitahara, *Adv. Colloid Interface Sci.*, 1980, **12**, 109–140.
33 D. M. Zhu, K. I. Feng and Z. A. Schelly, *J. Phys. Chem.*, 1992, **96**, 2382–2385.
34 T. Kluge, H. Knoll and M. Helmstedt, *Ber. Bunsen-Ges. Phys. Chem.*, 1997, **101**, 1703–1705.

35 K. Das, B. Jain and H. S. Patel, *Spectrochim. Acta, Part A*, 2004, **60**, 2059–2064.
36 E. E. Dormidontova, *Macromolecules*, 2002, **35**, 987–1001.
37 Y. I. Churakhina, Y. B. Ivanova, O. V. Maltzeva and N. Z. Mamardashvili, *Russ. J. Coord. Chem.*, 2009, **35**, 850–856.
38 M. Jayakannan and S. Ramakrishnan, *J. Polym. Sci., Part A: Polym. Chem.*, 2000, **38**, 2635–2644.
39 J. M. Wu, H. Yan, X. H. Zhang, L. Q. Wei, X. G. Liu and B. S. Xu, *J. Colloid Interface Sci.*, 2008, **324**, 167–171.
40 C. S. Lee, H. H. Chang, J. Jung, N. A. Lee, N. W. Song and B. H. Chung, *Colloids Surf., B*, 2012, **91**, 219–225.
41 A. R. Mustafina, J. G. Elistratova, O. D. Bochkova, V. A. Burilov, S. V. Fedorenko, A. I. Konovalov and S. Y. Soloveva, *J. Colloid Interface Sci.*, 2011, **354**, 644–649.
42 L. M. Qi, J. M. Ma and J. L. Shen, *J. Colloid Interface Sci.*, 1997, **186**, 498–500.
43 P. Gkolfi, D. Tsivaka, I. Tsougos, K. Vassiou, O. Malina, M. Polaskova, C. D. Polyzou, C. T. Chasapis and V. Tangoulis, *Dalton Trans.*, 2021, **50**, 13227–13231.
44 Z. Q. Wu, F. Yang, X. M. Li, A. Carroll, W. Loa-Kum-Cheung, H. M. Shewan, J. R. Stokes, D. Y. Zhao and Q. Li, *Colloids Surf., A*, 2022, **634**, 127917–127924.
45 X. J. Zhou, W. T. Wong, M. D. Faucher and P. A. Tanner, *J. Solid State Chem.*, 2008, **181**, 3057–3064.
46 X. Y. Wang, Y. Yukawa and Y. Masuda, *J. Alloys Compd.*, 1999, **290**, 85–90.
47 M. Perrier, S. Kenouche, J. Long, K. Thangavel, J. Larionova, C. Goze-Bac, A. Lascialfari, M. Mariani, N. Baril, C. Guérin, B. Donnadieu, A. Trifonov and Y. Guari, *Inorg. Chem.*, 2013, **52**, 13402–13414.
48 S. G. Duyker, G. J. Halder, P. D. Southon, D. J. Price, A. J. Edwards, V. K. Peterson and C. J. Kepert, *Chem. Sci.*, 2014, **5**, 3409–3417.
49 Z. Mitróová, M. Mihalik, A. Zentko, M. Lukácová, M. Mihalik, J. Vejpravová and L. F. Kiss, *Czech J. Phys.*, 2004, **54**, D559–D562.[magn SmFe).
50 Y. F. Xia, J. J. Mo, Q. H. Zhang, M. Liu and A. G. Peng, *J. Electron. Mater.*, 2022, **51**, 7150–7155.